Article

# Resolving the Structure of Ligands Bound to the Surface of Superparamagnetic Iron Oxide Nanoparticles by High-Resolution Magic-Angle Spinning NMR Spectroscopy

Laura Polito, Miriam Colombo, Diego Monti, Sergio Melato, Enrico Caneva, and Davide Prosperi

*J. Am. Chem. Soc.*, **2008**, 130 (38), 12712-12724 • DOI: 10.1021/ja802479n • Publication Date (Web): 30 August 2008



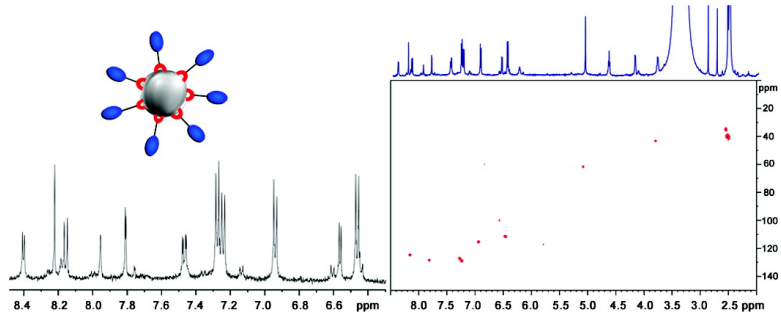


## More About This Article

Additional resources and features associated with this article are available within the HTML version:

- Supporting Information
- Access to high resolution figures
- Links to articles and content related to this article
- Copyright permission to reproduce figures and/or text from this article

View the Full Text HTML

J|A|C|S
ARTICLES

Published on Web 08/30/2008

# Resolving the Structure of Ligands Bound to the Surface of Superparamagnetic Iron Oxide Nanoparticles by High-Resolution Magic-Angle Spinning NMR Spectroscopy

Laura Polito, Miriam Colombo, Diego Monti, Sergio Melato, Enrico Caneva,* and Davide Prosperi*

*Department of Organic and Industrial Chemistry and Centro Interdipartimentale Grandi Apparecchiature, University of Milan, and Institute of Molecular Science and Technology, CNR, Milan, Italy*

Received April 4, 2008; E-mail: enrico.caneva@unimi.it (E.C.); davide.prosperi@unimi.it (D.P.)

***Abstract:*** A major challenge in magnetic nanoparticle synthesis and (bio)functionalization concerns the precise characterization of the nanoparticle surface ligands. We report the first analytical NMR investigation of organic ligands stably anchored on the surface of superparamagnetic nanoparticles (MNPs) through the development of a new experimental application of high-resolution magic-angle spinning (HRMAS). The conceptual advance here is that the HRMAS technique, already being used for MAS NMR analysis of gels and semisolid matrixes, enables the fine-structure-resolved characterization of even complex organic molecules bound to paramagnetic nanocrystals, such as nanosized iron oxides, by strongly decreasing the effects of paramagnetic disturbances. This method led to detail-rich, well-resolved $^{1}$H NMR spectra, often with highly structured first-order couplings, essential in the interpretation of the data. This HRMAS application was first evaluated and optimized using simple ligands widely used as surfactants in MNP synthesis and conjugation. Next, the methodology was assessed through the structure determination of complex molecular architectures, such as those involved in MNP3 and MNP4. The comparison with conventional probes evidences that HRMAS makes it possible to work with considerably higher concentrations, thus avoiding the loss of structural information. Consistent 2D homonuclear $^{1}$H−$^{1}$H and $^{1}$H−$^{13}$C heteronuclear single-quantum coherence correlation spectra were also obtained, providing reliable elements on proton signal assignments and carbon characterization and opening the way to $^{13}$C NMR determination. Notably, combining the experimental evidence from HRMAS $^{1}$H NMR and diffusion-ordered spectroscopy performed on the hybrid nanoparticle dispersion confirmed that the ligands were tightly bound to the particle surface when they were dispersed in a ligand-free solvent, while they rapidly exchanged when an excess of free ligand was present in solution. In addition to HRMAS NMR, matrix-assisted laser desorption ionization time-of-flight MS analysis of modified MNPs proved very valuable in ligand mass identification, thus giving a sound support to NMR characterization achievements.

## Introduction

A great spur in the progress of nanoscience has been elicited by the recent outstanding advances in the search for new materials with applications in biomedicine.[1] In this context, the fabrication of high-quality hybrid organic/inorganic nanoparticles endowed with distinguishable inherent optical and magnetic properties represents a promising new road to the development of a novel generation of diagnostic and therapeutic agents for biosensing, preclinical investigations, and clinical use.[2−5] In particular, superparamagnetic nanoparticles (MNPs) based on iron oxides hold tremendous potential biomedical applications thanks to a favorable combination of chemical and physical unique size-dependent properties, which are not observed at the molecular level or in the bulk phase, and to their satisfactory biocompatibility.[6−11] These nanoparticles have

(1) For recent reviews, see, for example: (a) Whitesides, G. M. *Nat. Biotechnol.* **2003**, *21*, 1161–1165. (b) Rosi, N. L.; Mirkin, C. A. *Chem. Rev.* **2005**, *105*, 1547–1562. (c) Katz, E.; Willner, I. *Angew. Chem., Int. Ed.* **2004**, *43*, 6042–6108. (d) Michalet, X.; Pinaud, F. F.; Bentolila, L. A.; Tsay, J. M.; Doose, S.; Li, J. J.; Sundaresan, G.; Wu, A. M.; Gambhir, S. S.; Weiss, S. *Science* **2005**, *307*, 538–544. (e) Sassolas, A.; Leca-Bouvier, B. D.; Blum, L. J. *Chem. Rev.* **2008**, *108*, 109–139. (f) Reiner, P. *Small* **2006**, *2*, 452–456. (g) Leroueil, P.; Hong, S.; Mecke, A.; Baker, J.; Orr, B.; Banaszak Holl, M. *Acc. Chem. Res.* **2007**, *40*, 335–342. (h) Yezhelyev, M. V.; Gao, X.; Xing, Y.; Al-Hajj, A.; Nie, S.; O'Regan, R. M. *Lancet Oncol.* **2006**, *7*, 657–667. (i) Peer, D.; Karp, J. M.; Hong, S.; Farokhzad, O. C.; Margalit, R.; Langer, R. *Nat. Nanotechnol.* **2007**, *2*, 751–760. (j) Fortina, P.; Kricka, L. J.; Surrey, S.; Grodzinski, P. *Trends Biotechnol.* **2005**, *23*, 168–173. (k) Minchin, R. *Nat. Nanotechnol.* **2008**, *3*, 12–13. (l) Ferrari, M. *Nat. Rev. Cancer* **2005**, *5*, 161–171. (m) Alivisatos, P. *Nat. Biotechnol.* **2004**, *22*, 47–52. (n) Medintz, I. L.; Uyeda, H. T.; Goldman, E. R.; Mattoussi, H. *Nat. Mater.* **2005**, *4*, 435–446.

(2) Weissleder, R.; Kelly, K.; Sun, E. Y.; Shtatland, T.; Josephson, L. *Nat. Biotechnol.* **2005**, *23*, 1418–1423.

(3) Veiseh, O.; Sun, C.; Gunn, J.; Kohler, N.; Gabikian, P.; Lee, D.; Bhattarai, N.; Ellenbogen, R.; Sze, R.; Hallahan, A.; Olson, J.; Zhang, M. *Nano Lett.* **2005**, *5*, 1003–1008.

(4) Zhao, M.; Kircher, M. F.; Josephson, L.; Weissleder, R. *Bioconjugate Chem.* **2002**, *13*, 840–844.

(5) Huh, Y.-M.; Lee, E. S.; Lee, J. H.; Jun, Y.-w.; Kim, P. H.; Yun, C. O.; Kim, J. H.; Suh, J. S.; Cheon, J. *Adv. Mater.* **2007**, *19*, 3109–3112.

(6) Gupta, A. K.; Gupta, M. *Biomaterials* **2005**, *26*, 3995–4021.



**10.1021/ja802479n CCC: $40.75** 

attracted a great deal of attention in cancer thermotherapy,[12,13] magnetic bioseparation,[14,15] cell targeting,[16−18] delivery,[19−22] and, especially, medical diagnostics because of their usefulness as contrast agents for magnetic resonance imaging (MRI)[23−29] and biosensing,[30−36] providing remarkable effects in signal reduction on $T_2$-weighted images. Another source of attractiveness resides in the relatively easy and straightforward functionalization of their hydroxyl-rich surface with organic molecules.[37] Nowadays, considerable synthetic advances have been achieved in interphase chemistry, providing a versatile synthetic platform for postfabrication core derivatization of nanocrystals, including MNPs, with (bio)organic molecules.[38−41] Such increasing synthetic potential actually will require very accurate, highly reliable, and possibly rapid methods for the structure-resolved characterization of surface organic molecules in the next future. Indeed, the major obstacle in developing superior molecular diversity of surface ligands resides in the inadequate reliability of current analytical methods for these substrates. In spite of numerous efforts, this objective still represents an open challenge in many instances. At present, X-ray photoelectron spectroscopy (XPS) and Fourier transform infrared (FTIR) spectroscopy are the preferred methods to check the presence of specific bonds and organic functional groups within the surface molecular coating.[42−44] Of course, such techniques offer a useful qualitative description of the presence of chemical species, but they are not appropriate for a structure-resolved identification of the organic layer on a molecular basis.

Usually, the structure of organic molecules in solution is accurately elucidated by $^1$H and $^{13}$C NMR spectroscopies combined with mass spectrometry. Unfortunately, performing NMR experiments with ligands supported on MNPs is complicated by large broadening effects deriving from the absence of ligand mobility on the crystal surface combined with field interferences caused by the material paramagnetism, which also measurably influences the nuclear magnetic relaxation of solvent nearby protons at distances up to 50 $\mu$m, resulting in a lack of any splitting of the peaks.[45] As a consequence, to obtain an appreciable set of signals in the $^1$H NMR spectrum, the solution has to be extremely dilute. For these reasons, the rare attempts reported in the literature with extremely dilute dispersions of MNPs bearing only unsophisticated ligands provided rather low spectral resolution lacking a well-defined first-order splitting pattern.[39,42] In principle, this difficulty might be overcome by reducing at the minimum the effect of magnetic nanodipoles caused by the presence of iron oxide crystals. For instance, $Fe_3O_4$ nanoparticles have been encapsulated within a thick silica shell to reduce the effect of the particle magnetization.[46]

The high-resolution magic-angle spinning (HRMAS) technique has been used successfully for the characterization of gels,[47] biopsies,[48] nanocrystalline proteins,[49] and metabolic phenotypes of entire microorganisms.[50] In a recent study, we


(7) Mornet, S.; Vasseur, S.; Grasset, F.; Duguet, E. *J. Mater. Chem.* **2004**, *14*, 2161–2175.
(8) Ito, A.; Shinkai, M.; Honda, H.; Kobayashi, T. *J. Biosci. Bioeng.* **2005**, *100*, 1–11.
(9) (a) Dobson, J. *Gene Ther.* **2006**, *13*, 283–287. (b) Jun, Y.-w.; Seo, J.-w.; Cheon, J. *Acc. Chem. Res.* **2008**, *41*, 179–189.
(10) Martina, M. S.; Fortin, J. P.; Menager, C.; Clement, O.; Barratt, G.; Grabielle-Madelmont, C.; Gazeau, F.; Cabuil, V.; Lesieur, S. *J. Am. Chem. Soc.* **2005**, *127*, 10676–10685.
(11) Jain, T. K.; Reddy, M. K.; Morales, M. A.; Leslie-Pelecky, D. L.; Labhasetwar, V. *Mol. Pharm.* **2008**, *5*, 316–327.
(12) Fortin, J. P.; Wilhelm, C.; Servais, J.; Menager, C.; Bacri, J. C.; Gazeau, F. *J. Am. Chem. Soc.* **2007**, *129*, 2628–2635.
(13) Samanta, B.; Yan, H.; Fischer, N. O.; Shi, J.; Jerry, D. J.; Rotello, V. M. *J. Mater. Chem.* **2008**, *18*, 1204–1208.
(14) El-Boubbou, K.; Gruden, C.; Huang, X. *J. Am. Chem. Soc.* **2007**, *129*, 13392–13393.
(15) Gu, H.; Xu, K.; Xu, C.; Xu, B. *Chem. Commun.* **2006**, 941–949.
(16) Josephson, L.; Tung, C. H.; Moore, A.; Weissleder, R. *Bioconjugate Chem.* **1999**, *10*, 186–191.
(17) Kohler, N.; Fryxell, G. E.; Zhang, M. *J. Am. Chem. Soc.* **2004**, *126*, 7206–7211.
(18) Babic, M.; Horak, D.; Trchova, M.; Jendelova, P.; Glogarova, K.; Lesny, P.; Herynek, V.; Hajek, M.; Sykova, E. *Bioconjugate Chem.* **2008**, *19*, 740–750.
(19) Gupta, A.; Curtis, A. *J. Mater. Sci.: Mater. Med.* **2004**, *15*, 493–496.
(20) Barnett, B. P.; Arepally, A.; Karmarkar, P. V.; Qian, D.; Gilson, W. D.; Walczak, P.; Howland, V.; Lawler, L.; Lauzon, C.; Stuber, M.; Kraitchman, D. L.; Bulte, J. W. M. *Nat. Med.* **2007**, *13*, 986–991.
(21) Chorny, M.; Polyak, B.; Alferiev, I. S.; Walsh, K.; Friedman, G.; Levy, R. J. *FASEB J.* **2007**, *21*, 2510–2519.
(22) Yoon, T.-J.; Kim, J. S.; Kim, B. G.; Yu, K. N.; Cho, M.-H.; Lee, J.-K. *Angew. Chem., Int. Ed.* **2005**, *44*, 1068–1071.
(23) Kircher, M. F.; Mahmood, U.; King, R. S.; Weissleder, R.; Josephson, L. *Cancer Res.* **2003**, *63*, 8122–8125.
(24) Harisinghani, M. G.; Barentsz, J.; Hahn, P. F.; Deserno, W. M.; Tabatabaei, S.; van de Kaa, C. H.; de la Rosette, J.; Weissleder, R. *N. Engl. J. Med.* **2003**, *348*, 2491–2499.
(25) de Vries, I. J. M.; Lesterhuis, W. J.; Barentsz, J. O.; Verdijk, P.; van Krieken, J. H.; Boerman, O. C.; Oyen, W. J. G.; Bonenkamp, J. J.; Boezeman, J. B.; Adema, G. J.; Bulte, J. W. M.; Scheenen, T. W. J.; Punt, C. J. A.; Heerschap, A.; Figdor, C. G. *Nat. Biotechnol.* **2005**, *23*, 1407–1413.
(26) Sosnovik, D. E.; Weissleder, R. *Curr. Opin. Biotechnol.* **2007**, *18*, 4–10.
(27) Corr, S. A.; Byrne, S. J.; Tekoriute, R.; Meledandri, C. J.; Brougham, D. F.; Lynch, M.; Kerskens, C.; O'Dwyer, L.; Gun'ko, Y. K. *J. Am. Chem. Soc.* **2008**, *130*, 4214–4215.
(28) Hoehn, M.; Kustermann, E.; Blunk, J.; Wiedermann, D.; Trapp, T.; Wecker, S.; Focking, M.; Arnold, H.; Hescheler, J.; Fleischmann, B. K.; Schwindt, W.; Buhrle, C. *Proc. Natl. Acad. Sci. U.S.A.* **2002**, *99*, 16267–16272.
(29) Evgenov, N. V.; Medarova, Z.; Dai, G.; Bonner-Weir, S.; Moore, A. *Nat. Med.* **2006**, *12*, 144–148.
(30) Perez, J. M.; Josephson, L.; O'Loughlin, T.; Hogemann, D.; Weissleder, R. *Nat. Biotechnol.* **2002**, *20*, 816–820.
(31) Perez, J. M.; Josephson, L.; Weissleder, R. *ChemBioChem* **2004**, *5*, 261–264.
(32) Taktak, S.; Sosnovik, D.; Cima, M. J.; Weissleder, R.; Josephson, L. *Anal. Chem.* **2007**, *79*, 8863–8869.
(33) Perez, J. M.; O'Loughin, T.; Simeone, F. J.; Weissleder, R.; Josephson, L. *J. Am. Chem. Soc.* **2002**, *124*, 2856–2857.
(34) Hsing, I.-M.; Xu, Y.; Zhao, W. *Electroanalysis* **2007**, *19*, 755–768.
(35) Stoeva, S. I.; Lee, J. S.; Smith, J. E.; Rosen, S. T.; Mirkin, C. A. *J. Am. Chem. Soc.* **2006**, *128*, 8378–8379.
(36) Stoeva, S. I.; Lee, J.-S.; Thaxton, C. S.; Mirkin, C. A. *Angew. Chem., Int. Ed.* **2006**, *45*, 3303–3306.
(37) Shultz, M. D.; Reveles, J. U.; Khanna, S. N.; Carpenter, E. E. *J. Am. Chem. Soc.* **2007**, *129*, 2482–2487.
(38) Polito, L.; Monti, D.; Caneva, E.; Delnevo, E.; Russo, G.; Prosperi, D. *Chem. Commun.* **2008**, 621–623.
(39) White, M. A.; Johnson, J. A.; Koberstein, J. T.; Turro, N. J. *J. Am. Chem. Soc.* **2006**, *128*, 11356–11357.
(40) Lee, K. S.; Lee, I. S. *Chem. Commun.* **2008**, 709–711.
(41) Lattuada, M.; Hatton, T. A. *Langmuir* **2007**, *23*, 2158–2168.
(42) Willis, A. L.; Turro, N. J.; O'Brien, S. *Chem. Mater.* **2005**, *17*, 5970–5975.
(43) Liang, Y. Y.; Zhang, L. M. *Biomacromolecules* **2007**, *8*, 1480–1486.
(44) Zhenghe, X.; Qingxia, L.; Finch, J. A. *Appl. Surf. Sci.* **1997**, *120*, 269–278.
(45) Sillerud, L. O.; McDowell, A. F.; Adolphi, N. L.; Serda, R. E.; Adams, D. P.; Vasile, M. J.; Alam, T. M. *J. Magn. Reson.* **2006**, *181*, 181–190.
(46) Guin, D.; Manorama, S. V. *Mater. Lett.* **2008**, *62*, 3139–3142.
(47) Händel, H.; Gesele, E.; Gottschall, G.; Albert, K. *Angew. Chem., Int. Ed.* **2003**, *42*, 438–442.
(48) Cheng, L. L.; Ma, M. J.; Becerra, L.; Ptak, T.; Tracey, I.; Lackner, A.; Gonzalez, R. G. *Proc. Natl. Acad. Sci. U.S.A.* **1997**, *94*, 6408–6413.
(49) Franks, W. T.; Wylie, B. J.; Schmidt, H. L. F.; Nieuwkoop, A. J.; Mayrhofer, R.-M.; Shah, G. J.; Graesser, D. T.; Rienstra, C. M. *Proc. Natl. Acad. Sci. U.S.A.* **2008**, *105*, 4621–4626.
(50) Blaise, B. J.; Giacomotto, J.; Elena, B.; Dumas, M.-E.; Toulhoat, P.; Segalat, L.; Emsley, L. *Proc. Natl. Acad. Sci. U.S.A.* **2007**, *104*, 19808–19812.

have shown that HRMAS could be a clever means to improve the low resolution in the $^1$H NMR spectra of organic solutes in neat ionic liquids (ILs), solving the effects of their magnetic susceptibility and remarkable viscosity.[51] This is in accordance with previous observations that the various sources of NMR interferences, including the anisotropy of magnetic susceptibilities, chemical shifts, and dipolar interactions, are averaged to their isotropic contributions or completely removed to produce spectra with enhanced sharp resonances.[52] On this basis, we reasoned that the HRMAS properties might be able to gain resolution with magnetic nanohybrids, not only by overcoming the problems associated with chemical shift anisotropy, but also by decreasing the broadening paramagnetic effects of iron oxide nanoparticles. In this context, we have recently anticipated that HRMAS allowed us to obtain quite narrow and split signals relative to that of the anomeric proton of the carbohydrate moieties of magnetic glyconanoparticles.[38] In the present paper, we demonstrate that HRMAS NMR has the potential to provide a robust device for the direct structure-resolved characterization of organic molecules stably anchored onto the paramagnetic surface of MNPs, avoiding ligand removal or particle decomposition. We set up a routine use of HRMAS experiments enabling precise and straightforward NMR analyses, including 1D $^1$H NMR, 2D homonuclear $^1$H−$^1$H correlation spectroscopy (COSY), and heteronuclear single-quantum coherence $^1$H−$^{13}$C (HSQC) experiments. To this aim, we carefully analyzed four samples characterized by increasing structural complexity, evaluating the dominant experimental conditions making this method successful.

On the other hand, magnetic beads were recently exploited as supporting matrixes for adsorbed bioorganic molecules in matrix-assisted laser desorption ionization time-of-flight (MALDI-TOF) experiments using commonly available instruments.[53] Hence, we explored the possibility of performing MALDI analyses directly on organic ligands bound to the MNP surface. This supplemental analytical tool provides further helpful support to the structure determination of hybrid MNPs.

## Experimental Section

**Materials and Methods.** All chemicals were purchased from Fluka (St. Gallen, Switzerland) and Riedel-de Haën (Seelze, Germany) and used as received. Water was deionized and ultrafiltered by a Milli-Q apparatus from Millipore Corp. (Billerica, MA) before use. $^1$H and $^{13}$C NMR spectra of compounds **1**−**4** were recorded on a Bruker Avance 400 instrument in the appropriate deuterated solvents with chemical shifts referenced to internal standards. The signals were assigned by means of APT, $^1$H−$^1$H COSY, and $^1$H−$^{13}$C HSQC spectra. Fourier-transformed infrared spectroscopy characterization was performed with a JASCO 300E FTIR instrument. Powder samples were pelleted with KBr at 8 tons, and the pellets were examined in the range between 4000 and 400 cm$^{-1}$.

HRMAS NMR experiments were carried out on a Bruker BioSpin FT-NMR Avance 500 equipped with a 11.7 T superconducting ultrashield magnet. The HRMAS probe with an internal lock is capable of performing either direct or indirect (inverse) detection experiments. MAS experiments were performed at spinning rates of up to 15 kHz (15 kHz maximum MAS rotation available) using a 50 $\mu$L zirconia rotor. All the samples were diluted at different concentrations with deuterated solvents to find the concentration limit to the NMR signal broadening. In general, we found that the best concentration optimizing the signal intensity vs particle dispersibility ratio was on the order of 1−2 mg/mL. However, concentrations of up to 4−5 mg/mL are permitted in principle, depending on the particle solubility. Proton spectra were obtained using 200−400 scans for each experiment. The sample temperature is dependent on the rotation speed, and it so varied. All the DOSY (diffusion-ordered spectroscopy) NMR spectra were acquired with the HRMAS probe, equipped with a pulsed gradient unit capable of producing magnetic field pulse gradients of 53.5 G cm$^{-1}$ in the $z$-direction. The MAS speed was 8 kHz and the approximate temperature was 305 K in each experiment. Bipolar gradient pulses were used for diffusion using two spoil gradients.[54] The duration of the magnetic field pulse gradients ($\delta$) was optimized for each diffusion time ($\Delta$) to obtain a 1−5% residual signal with the maximum gradient strength. In each PFG-NNR (pulsed-field gradient NMR) experiment, a series of 16−32 spectra on 16K data points were collected and the eddy current delay ($T_e$) was set to 5 ms. The value of $\delta$ was 1 ms, while the value of $\Delta$ was set between 10 and 30 ms; the pulse gradients ($g$) were incremented from 2% to 95% of the maximum gradient strength in a linear ramp. After Fourier transformation and baseline correction, the diffusion dimension was processed with the Bruker Xwin NMR software package (version 3.1).

For transmission electron microscopy (TEM) analysis, the MNP dispersion was diluted to ca. 0.1 mg/mL with hexane or ethanol and a drop was placed on a Formvar/carbon-coated copper grid and dried. TEM images were obtained by a Zeiss EM-109 microscope operating at 80 kV, available at the Sacco Hospital (Milan). Dynamic light scattering (DLS) measurements were performed using a Brookhaven 90Plus particle size analyzer working at 15 mW of a solid-state laser. MALDI-TOF MS experiments were performed in the linear mode on a Bruker Daltonics Microflex LT instrument equipped with a 337 nm nitrogen laser, working with a microSCOUT ion source positioned within the MALDI target.

**Synthesis of $Fe_3O_4$ Nanoparticles by the Coprecipitation Method.** Magnetite particles were obtained as previously described with minor modifications.[55] Briefly, 20 mL of a 1 M aqueous solution of $FeCl_3 \cdot 6H_2O$ and 5 mL of 2 M $FeSO_4 \cdot 7H_2O$ in 2 M HCl were added to 250 mL of 0.75 M ammonium hydroxide (25%) under vigorous mechanical stirring. The solution turned black almost instantaneously, and stirring was continued for 20 min. The particles were recovered with the help of a rare-earth permanent magnet, while the supernatant was discarded. The particulate was washed several times with distilled water and once with ethanol. Finally, the ethanol was discarded, and the particles were dried under vacuum.

**Sonochemical Functionalization of $Fe_3O_4$ Nanoparticles.** Previously exsiccated bare $Fe_3O_4$ nanoparticles (5 mg) were suspended in 5 mL of a 1% solution of the required ligand in the appropriate solvent (hexane or ethanol) under an argon atmosphere. The resulting unstable dispersion was sonicated for ca. 1 h at room temperature, until a homogeneous black suspension was obtained. The mixture was then centrifuged at 6000 rpm for 30 min and the solvent discarded. The collected black precipitate was redispersed, and three centrifugation/redispersion cycles afforded the modified nanoparticles free of reactant excess, which were dried under vacuum to remove the solvents before NMR analyses.

**Synthesis of Surfactant-Coated $Fe_3O_4$ Nanoparticles by Solvothermal Decomposition.** Highly monodisperse 5 nm $Fe_3O_4$ nanoparticles were obtained by the method developed by Sun and co-workers.[56] A 4 mmol sample of Fe(acac)$_3$ was dissolved in a

(51) Rencurosi, A.; Lay, L.; Russo, G.; Prosperi, D.; Poletti, L.; Caneva, E. *Green Chem.* **2007**, *9*, 216–218.
(52) Piotto, M.; Elbayed, K.; Wieruszeski, J. M.; Lippens, G. *J. Magn. Reson.* **2005**, *173*, 84–89.
(53) Lin, P.-C.; Tseng, M.-C.; Su, A.-K.; Chen, Y.-J.; Lin, C.-C. *Anal. Chem.* **2007**, *79*, 3401–3408.
(54) Wu, D.; Chen, A.; Johnson, C. S., Jr *J. Magn. Reson.* **1995**, *115*, 260–264.
(55) Yu, S. Y.; Zhang, H. J.; Yu, J. B.; Wang, C.; Sun, L. N.; Shi, W. D. *Langmuir* **2007**, *23*, 7836–7840.

***Scheme 1.*** Surface Functionalization of Iron Oxide Nanoparticles

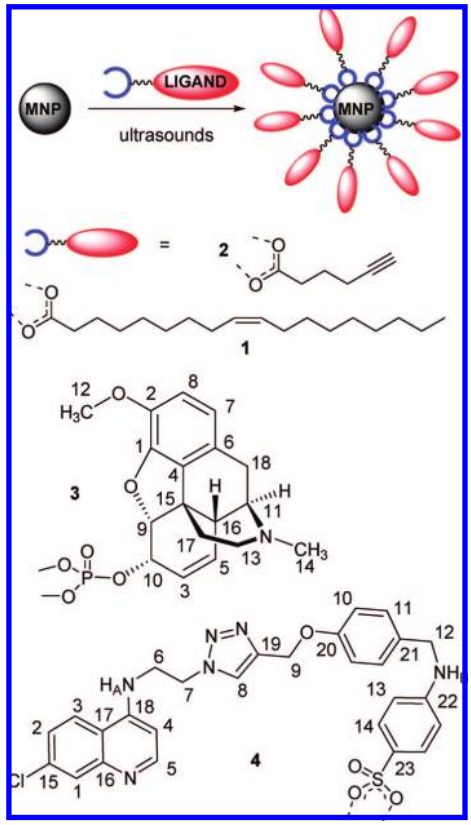


mixture of oleylamine (20 mL) and benzyl ether (20 mL). The mixture was dehydrated by being heated at 110 °C under nitrogen flux for 1 h. Then, the solution was quickly heated to reflux (300 °C), kept at this temperature for 2 h, and finally cooled to room temperature. Ethanol (100 mL) was then added under stirring, and the black precipitate was centrifuged. The supernatant was discarded, and the product was washed three times with ethanol to remove the unbound surfactant, providing 329 mg of approximately spherical, surfactant-coated magnetite nanocrystals. A representative TEM and DLS characterization of freshly prepared MNPs in hexane is included in the Supporting Information (Figure S1). The particles (2−3 mg) were finally resuspended in deuterated solvents, filtered through syringe PTFE 200 $\mu$m pore septa, and used for the HRMAS NMR experiments.

## Results and Discussion

**MNP Synthesis and Functionalization.** Nearly monodisperse 7 ± 3 nm magnetite nanoparticles were prepared by conventional coprecipitation of $Fe^{2+}$ and $Fe^{3+}$ ions in an alkaline medium, as previously reported,[54] and dried. Particle surface functionalization was achieved by ultrasonicating an MNP dispersion in a solution of the desired coordinating ligand dissolved in the appropriate organic solvent. After ligand binding to the particle surface, the nonreacted excess of organic material was removed by repeated centrifugation/resuspension cycles. We used four different organic ligands (**1**−**4**) outlined in Scheme 1, each one of them bearing a functional group with high affinity for surface iron hydroxyls—namely, carboxyl, sulfonate, and phosphate groups—for permanent particle grafting, thus obtaining the respective functionalized MNPs (MNP1−4). Oleic acid (**1**) was chosen because it is commonly employed as a coordinating surfactant during MNP fabrication by thermal decomposition carried out in organic solvents.[56,57] Different from that situation, the postsynthetic grafting procedure used in this work does not need to reach critical temperatures, and therefore, it should ensure the maintenance of the original *Z* configuration of the double bond at the 9,10-position of the alkyl chain. To assess the predicted differences between the ligand characteristics within these two distinct preparative methods, surfactant-coated 5 nm MNPs were also fabricated in organic solvents by high-temperature thermal decomposition of iron(III) acetylacetonate in the presence of an excess of oleylamine. Hexynoic acid (**2**) is a profunctional ligand of potential utility for azide−alkyne "click" (bio)conjugation due to the presence of the acetylene terminal group. Moreover, **2** has been previously investigated in pioneering $^1$H NMR investigations of organic-functionalized iron oxide NPs.[39] Ligands **3** and **4** are compounds of pharmacological interest, the polycyclic analgesic codeine phosphate, obtained by hydroxyl phosphorylation of commercial codeine, and a synthetic quinoline derivative, respectively. With these two definitely more sophisticated structural motifs, a more complicated splitting pattern was expected in $^1$H spectra, owing to the display of numerous sources of molecular complexity, including elements of defined stereochemistry, variably substituted aromatic rings, and the presence of heteroatoms. Compound **4** has potential as an antimalarial agent, and it was synthesized starting from *N*-(hydroxyethyl)-4-amino-7-chloroquinoline.[58] Its preparation and biological activity will be the subject of a future paper.

**Sample Preparation and Experimental Setup.** The HRMAS probes have been designed to perform solution-type experiments while the sample is spun at the "magic angle". The probe is doubly tuned ($^1$H and $^{13}$C), in addition to a $^2$H lock channel. All three channels operate via a single NMR transmit/receive solenoid coil located inside the MAS turbine, which is capable of performing either direct or inverse detection experiments. This system allowed us to perform high-resolution MAS experiments with 4 mm zirconia rotors at spinning rates of up to 15 kHz, using liquid or liquidlike samples. In this work, the spinning rates were optimized (often in the range 5−8 kHz) to reach a good compromise among the needs to have the spinning sidebands out of the $^1$H spectrum, the best resolution, and minimal disturbances from rotational artifacts. All the samples were suspended in deuterated solvents, such as benzene ($C_6D_6$), methanol ($CD_3OD$), and dimethyl sulfoxide (DMSO-$d_6$), mixed, sonicated, filtered through PTFE 200 $\mu$m pore septa to remove the large agglomerates, and finally diluted at different levels to find the concentration limit before the broadening of the NMR signals. In some cases, the filtration step was replaced by decanting the nanoparticle dispersion to precipitate the large aggregates and taking the upper suspension for analysis. The same sample solution that showed a resolved $^1$H NMR spectrum with HRMAS gave instead a wide broadened spectrum with a conventional 5 mm probe (QNP), thus demonstrating that those higher concentrations permitted with the HRMAS probe are not allowed with traditional NMR experiments (see Figure S9 in the Supporting Information). The sample temperature is MAS rate-dependent and so varied from 302 to 313 K, depending on the experiment performed.

(56) Xie, J.; Xu, C. J.; Xu, Z. C.; Hou, Y. L.; Young, K. L.; Wang, S. X.; Pourmand, N.; Sun, S. H. *Chem. Mater.* **2006**, *18*, 5401–5403.
(57) Hyeon, T.; Lee, S. S.; Park, J.; Chung, Y.; Na, H. B. *J. Am. Chem. Soc.* **2001**, *123*, 12798–12801.
(58) Melato, S.; Coghi, P.; Basilico, N; Prosperi, D.; Monti, D. *Eur. J. Org. Chem.* **2007**, 6118–6123.

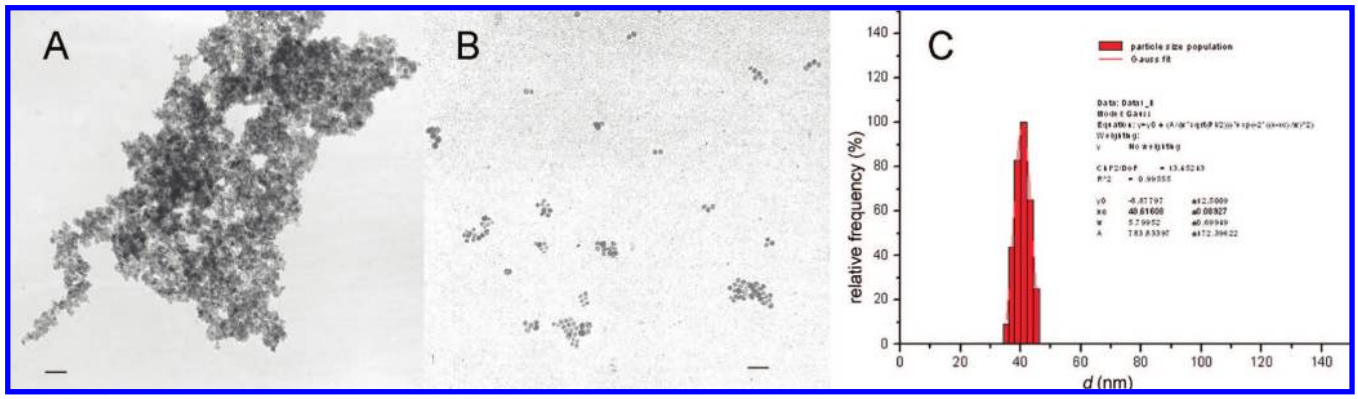


***Figure 1.*** Transmission electron micrograph of (A) an aqueous dispersion of as-synthesized, bare $Fe_3O_4$ nanoparticles, obtained by coprecipitation of $Fe^{2+}$ and $Fe^{3+}$ salts and (B) MNP1 in hexane (scale bars 30 nm). (C) Size distribution of a dispersion of MNP1 in hexane as estimated by DLS by fitting the experimental autocorrelation functions with a single-exponential decay: the mean value has been determined by a Gaussian fit of the relative intensities of the detected size populations.

Once the optimal parameters were fitted, we recognized some general recurring marks, which should be taken into account before any measurement is started. As a matter of fact, whatever the solvent, the $^1$H NMR spectrum of bare iron oxide nanoparticles presented a set of broad peaks ranging between 0.5 and 1.5 ppm. These signals are probably attributable to the presence of surface hydroxyls, water molecules trapped on the particle surface, and other uncheckable phenomena. It has been shown, indeed, that water molecules hold onto the iron oxide surface tenaciously.[59] Fortunately, such signals fall within a restricted range of chemical shifts, which, in general, is not diagnostic for organic molecules. In addition, it should be noticed that any reversibly adsorbed impurities—due to traces of residual solvents, side product formation during sonochemical reactions, or the use of raw materials—are also detectable, since no particular care was taken in removing minor molecular entities.

The MNP sample targets for MALDI-TOF experiments were prepared first by suspending the functionalized MNPs in the appropriate solvents (methanol for MNP3 or water and aqueous trifluoroacetic acid for MNP4) and then by short sonication and centrifugation to separate the precipitated MNPs. A mixture of the matrix (2,5-dihydroxybenzoic acid, 2 $\mu$L) and the target (2 $\mu$L) was spotted onto the sample plate, air-dried, and finally analyzed by MALDI-TOF MS.

**HRMAS NMR Analyses of Iron Oxide−Oleic Acid (MNP1) and Iron Oxide−Hexynoic Acid (MNP2).** Our aim in the first set of experiments was to establish the preponderant factors at play. To evaluate the incidence of solvent polarity on the quality of the spectral profiles, we performed HRMAS experiments on MNP1 and MNP2 in both $C_6D_6$ and DMSO. The TEM images in Figure 1 show the comparison between the as-synthesized bare nanoparticles and MNP1, highlighting that, once the particles were properly coated with the appropriate ligands and resuspended in the required solvent, each functionalized nanoparticle was singularly identified (Figure 1B). The hydrodynamic diameter of MNP1 was evaluated to make sure that what we were observing was effectively a colloidal dispersion rather than a particulate agglomeration. Assuming a refractive index of 2.42 for magnetite, DLS measurements performed on a 0.1 mg/mL dispersion of MNP1 in hexane resulted in a size dispersion of 41 $\pm$ 5 nm (Figure 1C), consistent with a monomeric colloidal state of the particles.

In Figure 2A, the comparison between the $C_6D_6$ spectra of technical grade oleic acid in solution (**1**, upper spectrum) and bound to $Fe_3O_4$ (MNP1, lower spectrum) is shown. Although the main peaks attributable to the presence of oleic acid are recovered, the upfield region of the spectrum of MNP1 is extremely poor in resolution, while the multiplet corresponding to the 9,10 double bond is not visible. A 10 kHz MAS rate was indeed necessary to separate the signals from the background noise. In contrast, Figure 2B illustrates how the use of a much more polar, yet nonprotic, solvent provided an impressive improvement in signal narrowing. An MAS rate as low as 1 kHz was enough to achieve a good first-order signal display. However, we found that 5 kHz was the best choice to obtain clean, sideband-free peaks. Each signal was singularly distinguishable, and the peak multiplicities were unambiguously preserved. Moreover, the lowering of the MAS rate results in a more conservative distribution of the chemical shifts: in this case, the H9−H10 multiplet was found at 5.33 ppm, close to the corresponding value for **1** in solution.

To assess the generality of the method, we performed the same experiments on surfactant-coated 5 nm magnetite nanoparticles prepared by thermal decomposition carried out in benzyl ether (Figure 2C). As in the previous case, the particles were suspended in deuterated benzene (upper spectrum) or DMSO (lower spectrum) and the HRMAS spectra were acquired at 10 and 5 kHz MAS rates, respectively. The spectral profiles are very similar to those obtained with MNP1, although small differences are evident between the lower parts of panels B and C of Figure 2. In particular, in Figure 2C, the peak at 5.33 ppm corresponding to the double bond is extremely weak, and the relative intensities of the signals of the protons in the saturated aliphatic region are not respected. This is consistent with previous evidence on a substantial loss of unsaturation and changes in the structure of aliphatic long alkyl chains above 290 °C.[42]

NMR spectra of MNP2 were obtained under similar conditions, suspending the particles first in benzene and then in DMSO. The $C_6D_6$ $^1$H spectrum shows a broad unresolved set of signals ranging from 0.5 to 2.0 ppm, corresponding to the proton shifts of the hydrocarbon chain in that solvent, giving rise to an indistinct line shape very similar to that of MNP1. Analogously to MNP1, a markedly higher spin rate was needed (15 kHz), thus resulting in a significant upfield shifting of the entire group of signals with respect to the ligand in solution

(59) Navrotsky, A.; Mazeina, L.; Majzlan, J. *Science* **2008**, *319*, 1635–1638.

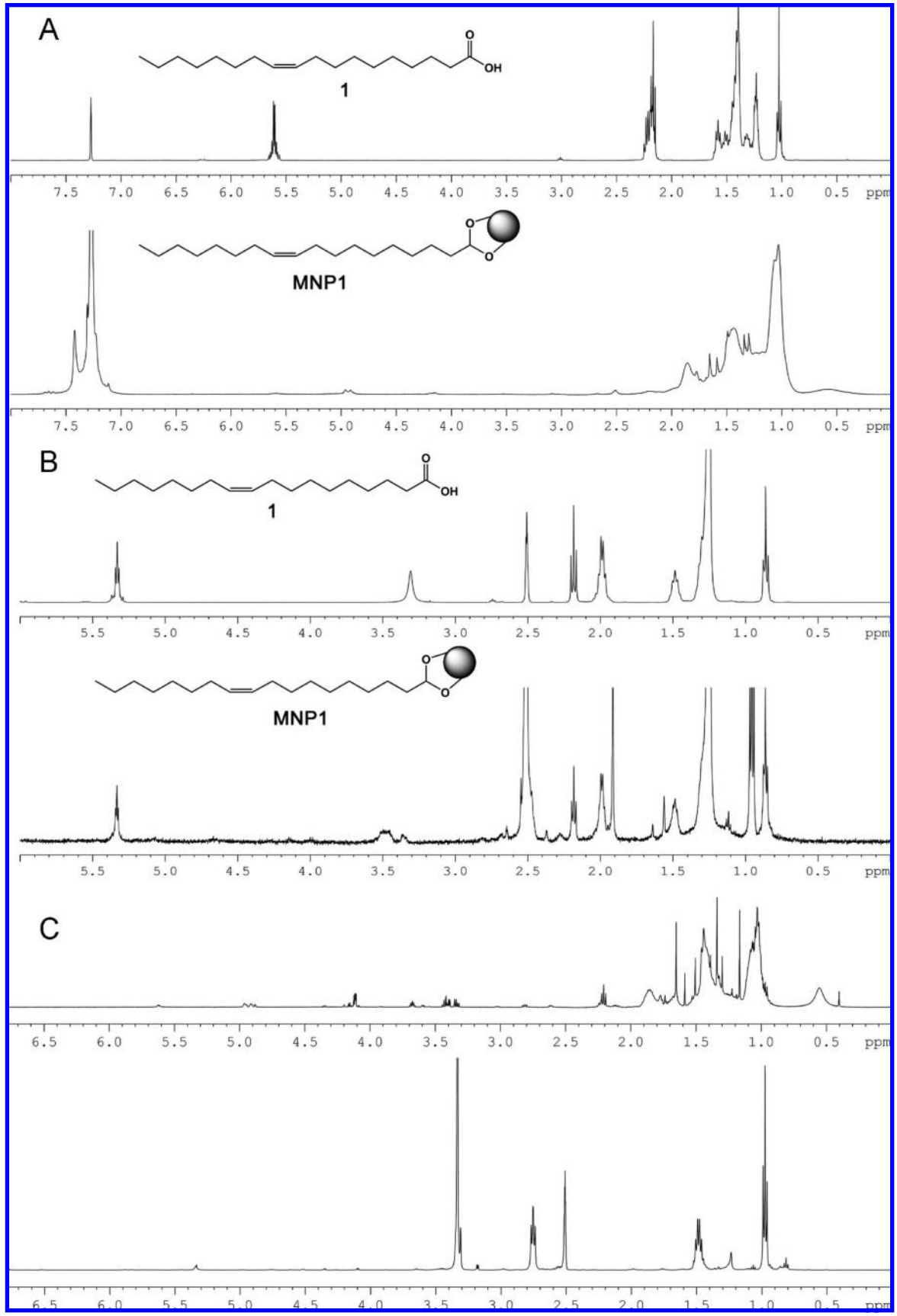


***Figure 2.*** Comparison between the $^1$H NMR spectrum of oleic acid in solution (**1**, upper spectrum) and the $^1$H HRMAS NMR spectrum of the ligand bound to MNPs (MNP1, lower spectrum) performed in (A) $C_6D_6$ at a 10 kHz MAS rate and (B) DMSO-$d_6$ at 5 kHz. (C) HRMAS $^1$H NMR spectra of surfactant-coated MNPs obtained by organic-phase solvothermal decomposition of iron(III) acetylacetonate performed in $C_6D_6$ (upper spectrum) at 10 kHz and DMSO-$d_6$ (lower spectrum) at a 5 kHz MAS rate.

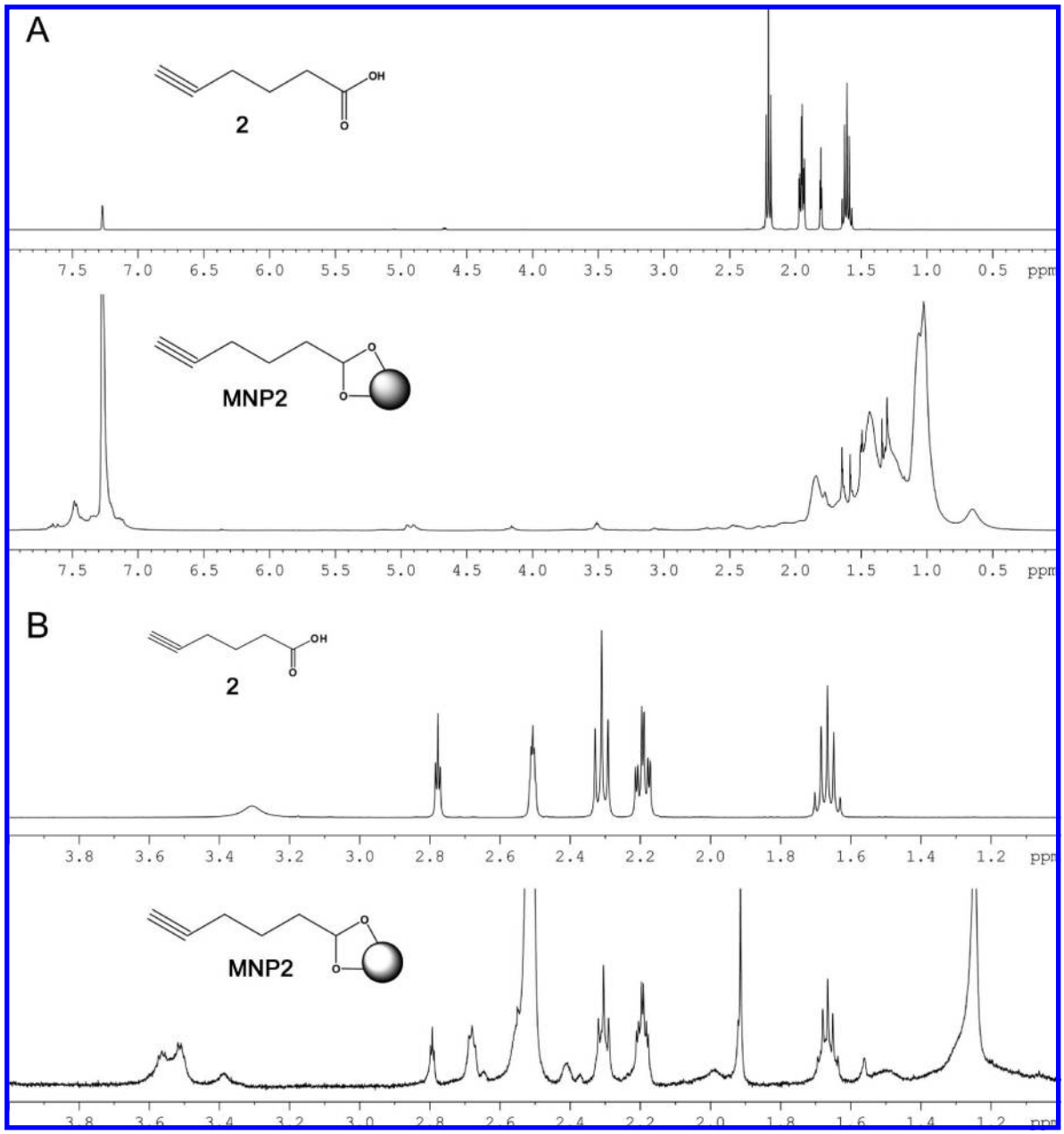


***Figure 3.*** Comparison between the $^{1}$H NMR spectrum of hexynoic acid in solution (**2**, upper spectrum) and the HRMAS spectrum of the ligand bound to MNPs (MNP2, lower spectrum) in (A) benzene at a 15 kHz MAS rate and (B) dimethyl sulfoxide at a 5 kHz MAS rate.

(Figure 3). Once again, by using DMSO as the solvent, the quality of signal resolution was radically improved. The original fine spectral profile was strictly maintained, both in regard to the chemical shifts of H2, H3, H4, and H6 and in regard to the respective multiplicities. Notably, a long-range spin coupling between the acetylenic H6 and the H4 position is clearly evidenced: H6, indeed, appears as a distinct triplet having a propargylic long-range $J_{6,4}$ of 2.6 Hz. The same H6 to H4 coupling was recovered within the $^{1}$H−$^{1}$H COSY experiment, together with H3−H4 and H4−H5 couplings (see Figure S2A in the Supporting Information). MNP2 was also successfully tested in 2D $^{1}$H−$^{13}$C correlation (HSQC) experiments (Figure S2B in the Supporting Information). Such a result highlights a further major achievement of this work. Actually, the low absolute analyte concentrations in suspension have rendered the acquisition of $^{13}$C NMR spectra of functionalized MNPs substantially prohibitive thus far. This experiment, instead, provided us with an indirect, yet reliable, $^{13}$C characterization of MNP-decorating ligands (complete NMR assignments for MNP2 are reported in the Supporting Information). Obviously, the limitation of the HSQC method is that it intrinsically lacks the identification of quaternary carbon atoms, such as C1 and C5. On the contrary, C2−C4 were unambiguously attributed, obtaining a full molecular NMR characterization for this anchored ligand.

Altogether, the above results highlight two major critical conditions for the successful performance of HRMAS NMR experiments on hybrid MNPs: (1) the characteristics of the analytical solvent and (2) the optimal angular frequency of the rotor containing the sample within the probe cavity. Of course, sample solubility in an appropriate solvent is required. However, we found that solvent polarity is much more crucial to obtain

narrow structure-resolved resonances, independent of concerns about the best order of solubility. The next paragraph of this paper is devoted to a more focused description of those aspects that are more strictly associated with the MAS rate of the sample.

**Effect of the MAS Rate.** In paramagnetic materials, the magnetic susceptibility $\chi > 0$, and it increases with an increase of the paramagnetic/superparamagnetic character, up to values higher than $10^3$ in ferromagnetic materials. When NMR spectra are acquired, the line shape resolution fwhm (full width at half-maximum) height of the $^1$H signals rapidly decreases in the presence of paramagnetic molecules, depending on the $\chi$ parameter, down to a limit corresponding to the complete disappearance of the NMR signals. Moreover, this line shape is inversely dependent on the spin−spin relaxation time $T_2$, and therefore, it is possible to raise the $T_2$ value again by increasing the tumbling rate of the sample molecules.[60] The susceptibility $\chi$ is also inversely dependent on the temperature $T$ (deduced from basic formulas derived from the Curie law: $\chi = C/T$, where $C$ is the Curie constant), and it is influenced by field ranges and other parameters of the specific model under investigation.[61] These indications corroborate our observations that an increment in molecular tumbling results in an effective decrease of the paramagnetic effects on the sample, working against the formation of wide dipolar magnetic domains. This evidence suggested to us that the use of the HRMAS probe could have a strong influence on both the $\chi$ and $T_2$ parameters, leading to an improvement in signal resolution and sensitivity. Indeed, on the basis of MAS theory, when the sample is rotated at the magic angle, the contribution to the additional magnetic field sensed by each individual paramagnetic element responsible for the signal broadening is strongly reduced, and in some cases it vanishes, while the spinning sidebands in the spectra are dependent on the rotation frequency.[62]

We have mentioned above the incidence of elevated MAS rates on proton chemical shifts. Sometimes, we noticed a nonspecific upfield shift in the signals under MAS rates above 10−12 kHz, independently of the influence of the electromagnetic neighborhood from each spinel. The MAS speed increment involves only a moderate change of the sample temperature, usually on the order of 1−1.5 K for a 1 kHz increment. For this reason, we observed some possible chemical shift variations only when working in the range 10−15 kHz (see, for instance, the upfield shifting in the hexynoic spectra, Figure 3A). More relevant, a centrifuge-like effect due to extremely elevated MAS rates in most cases resulted in an overall band broadening, owing to a turbulence increase. On the contrary, by working at the lowest rate values (under 1000 Hz), it was almost impossible to separate the signals from background noise, while at intermediate rates (1−3 kHz) pronounced sidebands often appeared beside the most intense peaks. The dependence of the sideband gap on the spinning rate is theoretically predicted,[62] and it has been experimentally observed with solid-state MAS NMR in a recent study on laponite and polystyrene powders containing traces of ferromagnetic particles.[63] Figure 4 gives an impression of this positive trend in the line shape of the NMR signals, the temperature changes being roughly negligible, thus demonstrating that the molecular tumbling increment is one of the predominant positive factors in signal separation. Preliminary experiments carried out on different samples suggest that, in most cases, the optimal working rate falls within 5 and 8 kHz, although we have little evidence that lower rates are allowed using ligands with higher molecular weights.

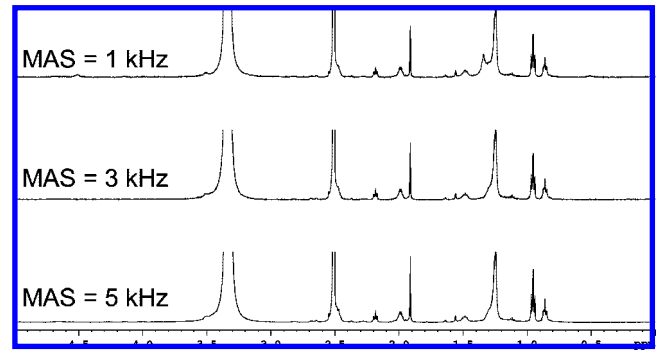


***Figure 4.*** Dependence of the $^1$H HRMAS NMR line shape in MNP1 spectra on the MAS rate increment. At 1 kHz, sideband artifacts are clearly visible, especially near the intense signal at 1.27 ppm corresponding to hydrocarbon chain protons.

In summary, our most plausible interpretation of the encouraging results presented in this paper is that the strong increment in the tumbling molecular rate, induced by the high-speed rotation of the rotor in the HRMAS probe at the magic angle, effectively works against the formation of wide dipolar magnetic domains, which otherwise provide the above-mentioned superparamagnetic broadening effects. Each experiment, however, needs to be carefully set up to find the optimal MAS speed, depending on the particulate stability and solvent polarity.

**Determining the Ligand Structure of MNP3 and MNP4 by HRMAS and MALDI-TOF.** With the optimized HRMAS methodology in hand, we then moved to the investigation of more complex molecular structures, such as those involved in the organic layers of MNP3 and MNP4. Codeine phosphate displays six stereochemically defined elements, namely, five asymmetric carbons and a *Z*-configured double bond within a condensed five-membered multiring (Scheme 1). We performed 1D $^1$H and 2D $^1$H−$^1$H COSY and $^1$H−$^{13}$C HSQC HRMAS experiments by suspending MNP3 in $CD_3OD$ at different MAS rates. Thanks to the excellent particle stability in methanol, in this case, we were allowed to reach 15 kHz without a detectable loss in spectral definition.

The comparison between the most interesting downfield regions of the $^1$H fingerprints of codeine phosphate (**3**) and MNP3 is shown in Figure 5. Although a residual small broadening effect is present in the MNP3 signals, the resulting splitting pattern is substantially conserved. Also the coupling constants follow those presented in the solute spectrum faithfully. This result, together with the COSY and HSQC data reported in Figure 6, allowed us to accurately elucidate the fine structure of the bound ligand. The attributed proton and carbon chemical shift assignments are summarized in Table 1. As expected, most signals are just slightly (0.02−0.05 ppm) upshifted, although more significant changes are recovered in the upfield region, especially for those protons which are involved in the highly constrained bridged ring. However, we may affirm that the original molecular fingerprint is essentially respected. The only remarkable difference emerges at the H11 chemical shift, which is significantly upshifted from 4.08 to 3.76

(60) Freeman, R., Ed. *Nuclear Magnetic Resonance*; Longman Scientific and Technical: Harlow, U.K., 1988; pp 264−265.
(61) Ponomarenko, L. A.; de Visser, A.; Bruck, E.; Tishin, A. M. April 27, 2001, arXiv:cond-mat/0104539. arXiv.org e-Print archive.
(62) Elbayed, K.; Dillmann, B.; Raya, J.; Piotto, M.; Engelke, F. *J. Magn. Reson.* **2005**, *174*, 2–26.
(63) Levin, E. M.; Bud'ko, S. L.; Mao, J. D.; Huang, Y.; Schmidt-Rohr, K. *Solid State NMR* **2007**, *31*, 63–71.

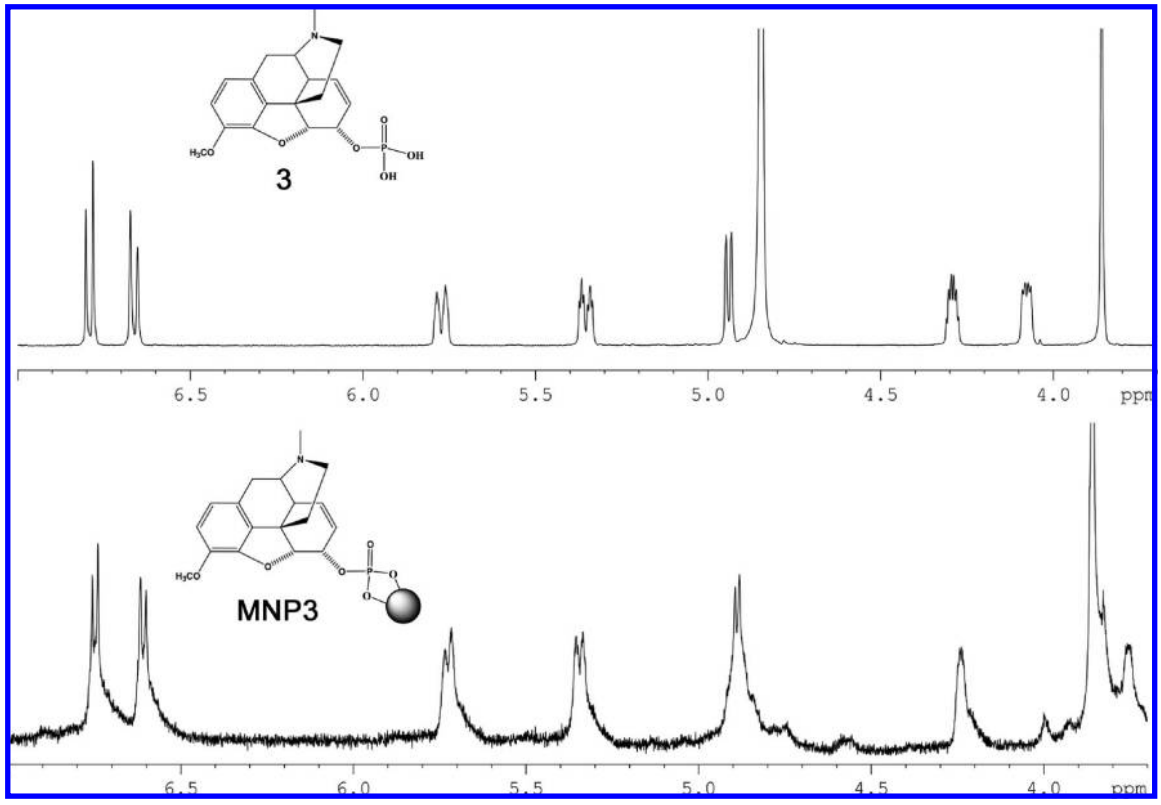


***Figure 5.*** Comparison between the downfield regions of the $^1$H NMR spectrum of codeine phosphate in $CD_3OD$ solution (**3**, upper spectrum) and the HRMAS spectrum of MNP3 (lower spectrum, $H_2O$-presaturated), performed at a 15 kHz MAS rate.

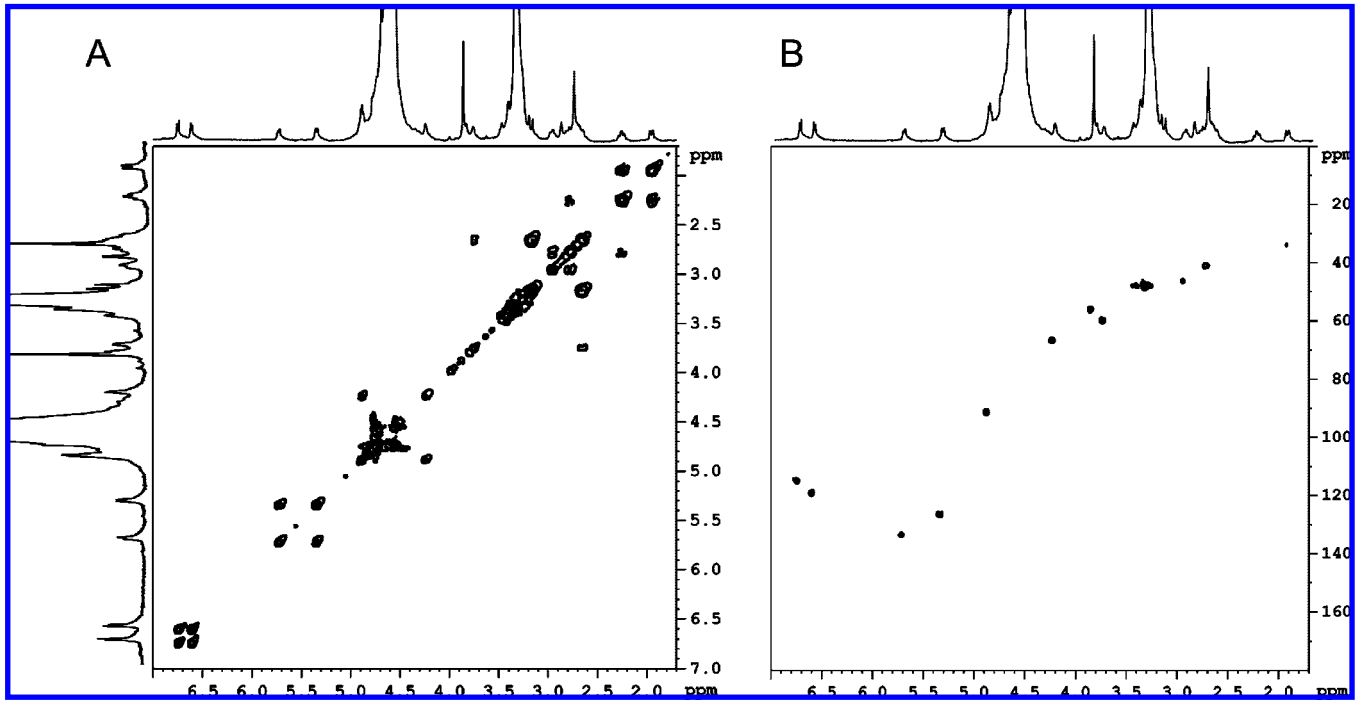


***Figure 6.*** 2D HRMAS NMR spectra of MNP3 acquired in $CD_3OD$: (A) $^1$H−$^1$H COSY, (B) $^1$H−$^{13}$C HSQC.

ppm. This anomalous behavior suggests that the anchored molecule is blocked in a fixed geometry on the particle surface, in which H11 is directed toward the field-shielding iron oxide core, on the same side of the phosphate group. A possible explanation for this might reside in the superparamagnetic properties of the iron core, which, once immersed in an external electromagnetic field, behaves like an oriented nanodipole, inducing a small shielding effect in an immediate neighborhood of the spinel surface. A more thorough insight into the spectrum fine structure highlights that the splittings are in good agreement with the expected peak shapes. The detectable coupling constants in the MNP3 spectrum were compared to those of **3** (these data

***Table 1.*** Comparison between the $^1$H and $^{13}$C NMR Shifts (ppm) of MNP3 and **3**

| H/C assignment | $^1$H, MNP3 | $^1$H, **3** | $\Delta\delta^a$ | | $^{13}$C, MNP3 | $^{13}$C, **3** |
|---|---|---|---|---|---|---|
| 3 | 5.34 | 5.35 | 0.01 | CH | 126.6 | 125.3 |
| 5 | 5.73 | 5.77 | 0.04 | CH | 133.6 | 133.8 |
| 7 | 6.61 | 6.66 | 0.05 | CH | 119.2 | 119.4 |
| 8 | 6.75 | 6.79 | 0.04 | CH | 115.1 | 114.6 |
| 9 | 4.89 | 4.94 | 0.05 | CH | 91.2 | 91.1 |
| 10 | 4.24 | 4.29 | 0.05 | CH | 66.7 | 66.4 |
| 11 | 3.76 | 4.08 | 0.32 | CH | 59.8 | 60.3 |
| 12 | 3.86 | 3.86 | 0.00 | $CH_3$ | 55.9 | 55.9 |
| 13 | 3.17, 2.86 | 3.26, 3.05 | 0.09, 0.19 | $CH_2$ | 45.7[b] | 46.6 |
| 14 | 2.73 | 2.97 | 0.24 | $CH_3$ | 40.9 | 40.2 |
| 16 | 2.95 | 3.12 | 0.17 | CH | 46.4 | 37.4 |
| 17 | 2.24, 1.95 | 2.47, 2.03 | 0.23, 0.08 | $CH_2$ | 33.7 | 32.2 |
| 18 | 3.19, 2.70 | 3.25, 2.88 | 0.06, 0.18 | $CH_2$ | 26.8[b] | 21.8 |

[a] Proton upfield shifting of ligand **3** as bound to MNPs with respect to the solution state. [b] These signals were very weak and were obtained by enhancing the spectral baseline; the accuracy for these values is low, since the signals are disturbed by background noise.

are included in Table S1 in the Supporting Information). Even though not completely resolved, the complex multiplicity of H5 and H10 allowed us to sense a ddd-like peak structure reminiscent of the respective splittings in solution. Likewise, the $^{13}$C chemical shifts of primary to ternary carbons inferred by HSQC were conserved to a great extent (Table 1 and Figure 6).

We acquired MALDI-TOF mass spectra of codeine phosphate (**3**) and codeine phosphate linked to MNPs (MNP3). The mass spectrum of **3** showed an intense peak at 297.9 *m*/*z* corresponding to codeine, losing the phosphate group (expected MW = 299.36). It is noteworthy to underline that an accurate calibration of the instrument is ensured when molecular weights larger than 400 are registered. The small discrepancy between the experimental data obtained and the exact molecular weight of codeine can find a reason in that. Notwithstanding, we acquired the mass spectra of MNP3, which confirmed the presence of codeine phosphate on the surface of magnetic nanoparticles. The spectrum actually showed an intense peak at 298.0 *m*/*z* congruent with the result obtained from the analysis of free ligand (Figure S4 in Supporting Information).

The $^1$H spectrum of the quinoline derivative **4** (see Scheme 1) in DMSO displays two sets of signals, the first including all aromatic protons within the range 9.2−6.5 ppm (Figure 7B), while nonaromatic H6, H7, H9, and H12 are located between 5.2 and 3.9 ppm. The comparison between parts A and B of Figure 7 highlights the differences in the $^1$H spectra of the aromatic region of **4** and MNP4, respectively, performed in DMSO. As in the previous example, the fine structure of the signals is well-resolved, especially in the downfield region, where coupling constants as low as 5.4 Hz ($J_{4,5}$) and 2.2 Hz ($J_{meta}$ between H1 and H2) are recovered. Compared to that of the MNP3 spectrum, the sharpness of the MNP4 signals is further enhanced, since also the peak line shape drift due to a residual $T_2$ effect in MNP3 signals is now completely absent. The line shape here has a resolution on the same order as that of the spectrum of **4** itself. Such an improvement is probably attributable to the positive effect of the polyaromatic system in the molecular backbone of **4**, which influences the effect of the nanodipole orientation, according to the well-known interaction of the local magnetic vector derived from the aromatic rings with the surrounding magnetic environment.

The complete assignments with the respective coupling constants are reported in Table 2, while Table S2 summarizes the main $^{13}$C NMR shifts (see the Supporting Information). It should be noted that also the peak integrals are in agreement with the respective values expected for the CH and $CH_2$ signals. Our attention was then captured by the anomalous shifting of some of the proton signals, particularly H2, H3, H6, and $NH_A$. Differently from the other signals, these peaks were unexpectedly upshifted (0.21−0.24 ppm for CH and 1.21 ppm for NH). We argued that they should feel the field-shielding effect of iron oxide clusters, similar to H11 in MNP3. Since all the protons involved in this upshifting phenomenon are close to the aminic nitrogen of the quinoline moiety, we propose an alternative model for binding of this ligand to the iron oxide surface, which is quite different from that represented in Scheme 1. Indeed, if both the sulfonate and the amino group were involved in particle hooking in a sort of bipod chelating, then H2, H3, and H6 would be confined in a close proximity to the iron-rich particle surface (Figure 8), thus providing a possible justification of the observed peak upshiftings. This hypothesis is further corroborated by the appreciable upfield shifting of H14 protons (0.06 ppm) with respect to H13 (0.01 ppm) and by the comparison between the behaviors of H6 (0.21 ppm upshift) and H10 (0.03 ppm downshift). Indeed, the methylene groups at the 6- and 10-positions are both adjacent to secondary anilinic amines. Therefore, if other factors are dominant, such as the nitrogen protonation states, these protons should experience the same shielding/deshielding effect depending on the respective nitrogen protonation, which is expected to be strictly similar. Moreover, it is well documented that the quinolinic nitrogen ($NH_A$) is extremely unreactive toward both protonation and alkylation,[64] while it is allowed to be involved in coordination with metals. On the other hand, our bipodal chelating model takes into account the fact that, while the $NH_A$ group is conformationally allowed to coordinate the iron surface, $NH_B$ is prevented from doing so by rigid geometrical constraints.

To have compelling evidence that our results refer to a hybrid system in which ligands are effectively anchored onto the particle surface, we performed two supplementary experiments with MNP4.

First, we acquired the HRMAS proton spectra of a mixture of MNP4 and a large excess of **4** in DMSO-$d_6$ under the same working conditions used for the experiments with pure MNP4 (Figure 7C). Quite surprisingly, we noticed that most signals, particularly those relative to protons more strongly affected by the particle surface, were recovered at intermediate values between the corresponding proton shifts in **4** and MNP4, respectively. This behavior may find a plausible explanation in the fact that, when an excess of ligand is present in solution, a very rapid exchange with the bound quinoline occurs. If such an event is faster than the acquisition time, the resulting spectral profile will be intermediate between the limit cases of **4** (Figure 7A) and MNP4 (Figure 7B), accounting for an averaged magnetic status experienced by each exchanging chemical species. This implies that, although the quinolinic ligand affinity is sufficiently high to avoid its displacement from the nanoparticle surface by the DMSO molecules, however, the linkage is not properly covalent, and it may be disrupted in the presence of ligands with comparable or higher affinity for iron oxide.

In a second complementary experiment, we compared the 2D diffusion resonance spectra of **4**, MNP4, and the mixture

(64) Kaschula, C. H.; Egan, T. J.; Hunter, R.; Basilico, N.; Parapini, S.; Taramelli, D.; Pasini, E.; Monti, D. *J. Med. Chem.* **2002**, *45*, 3531–3539.

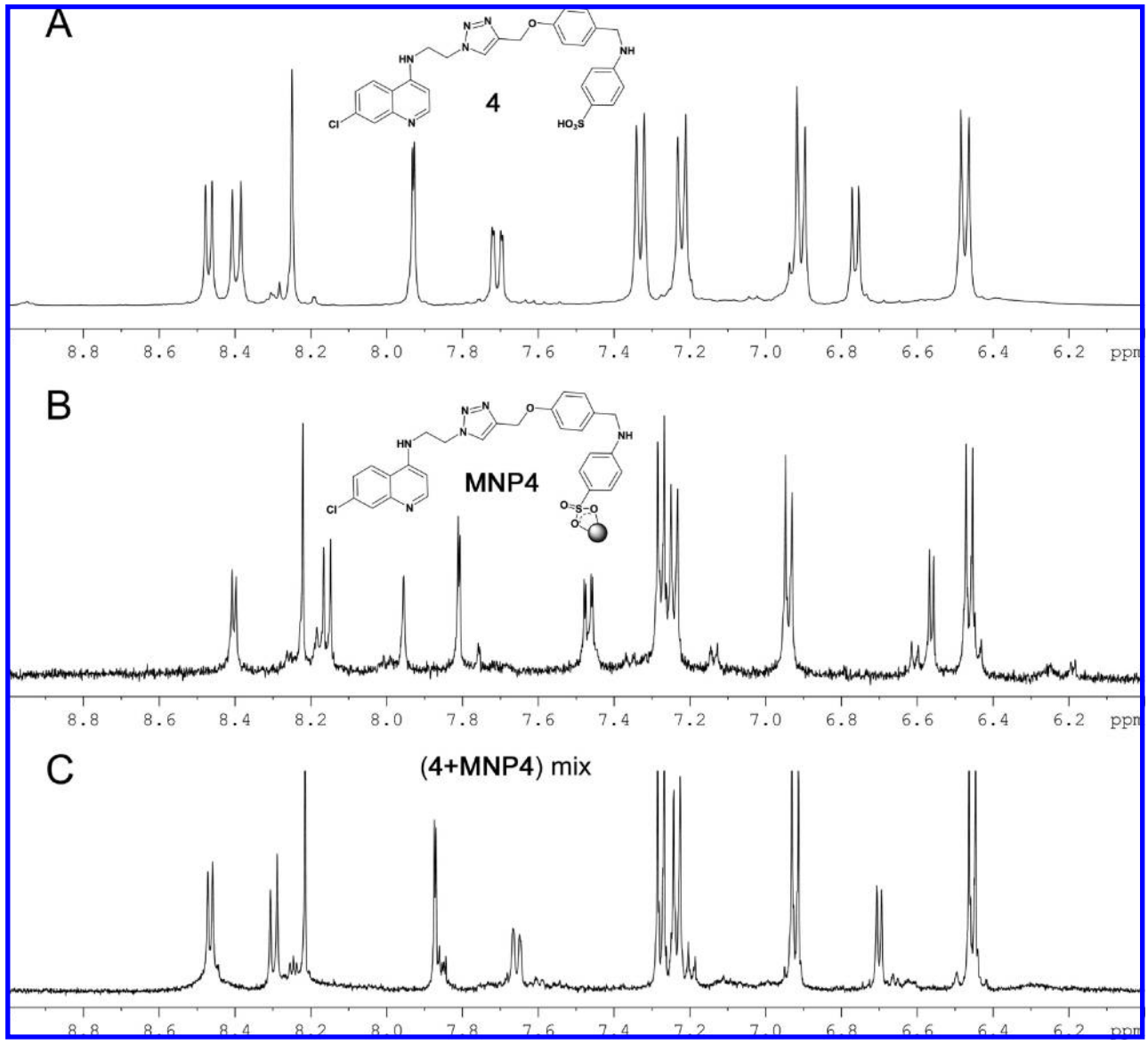


***Figure 7.*** Comparison among the downfield regions of (A) the $^1$H NMR spectrum of ligand **4** and (B, C) the $^1$H HRMAS NMR spectra of (B) MNP4 and (C) MNP4 + excess **4**, performed in dimethyl sulfoxide-$d_6$ at 8 kHz.

***Table 2.*** $^1$H NMR Chemical Shift Assignments and Coupling Constants of MNP4 and **4**

| | | | | multiplicity | | | |
|---|---|---|---|---|---|---|---|
| H assignment | $\delta$(MNP4) (ppm) | $\delta$(**4**) (ppm) | $\Delta\delta$[a] | MNP4 | **4** | $J$(MNP4) (Hz) | $J$(**4**) (Hz) |
| 1 | 7.81 | 7.93 | 0.12 | d | d | 2.2 | 2.0 |
| 2 | 7.47 | 7.71 | 0.24 | dd | dd | 2.2,9.1 | 2.0,9.1 |
| 3 | 8.16 | 8.39 | 0.23 | d | d | 9.1 | 9.1 |
| 4 | 6.56 | 6.76 | 0.20 | d | d | 5.4 | 6.9 |
| 5 | 8.40 | 8.47 | 0.07 | d | d | 5.4 | 6.9 |
| 6 | 3.80 | 4.01 | 0.21 | m | m | | |
| 7 | 4.66 | 4.72 | 0.06 | t | t | 5.9 | 6.0 |
| 8 | 8.22 | 8.24 | 0.02 | s | s | | |
| 9 | 5.08 | 5.05 | −0.03 | s | s | | |
| 10 | 6.94 | 6.91 | −0.03 | d | d | 8.7 | 8.6 |
| 11 | 7.24 | 7.21 | −0.03 | d | d | 8.7 | 8.6 |
| 12 | 4.19 | 4.19 | 0.00 | br d[b] | s | 5.3 | |
| 13 | 6.46 | 6.47 | 0.01 | d | d | 8.6 | 8.6 |
| 14 | 7.27 | 7.33 | 0.06 | d | d | 8.6 | 8.6 |
| $NH_A$ | 7.95 | 9.16 | 1.21 | br, s | m | | |

[a] Proton upfield shifting of ligand **4** as bound to MNPs with respect to the solution state. [b] Coupling between H12 and $NH_B$.

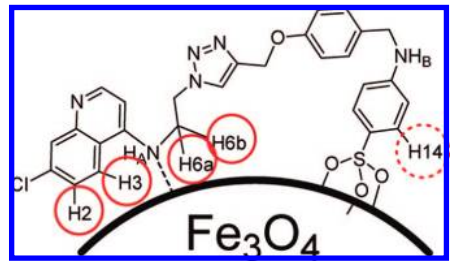


***Figure 8.*** Schematic representation of the proposed alternative model for binding of **4** to the magnetite surface, based on the experimental $^1$H NMR shifts. Red-circled protons are those directly involved in the shielding effect of the nanodipole, resulting in a significant (full outline) or slight (dashed outline) upfield shifting in the $^1$H spectrum, depending on the distance from the crystal surface. Within this bipodal chelating model, the molecule is prevented from freely rotating, having lost several degrees of freedom.

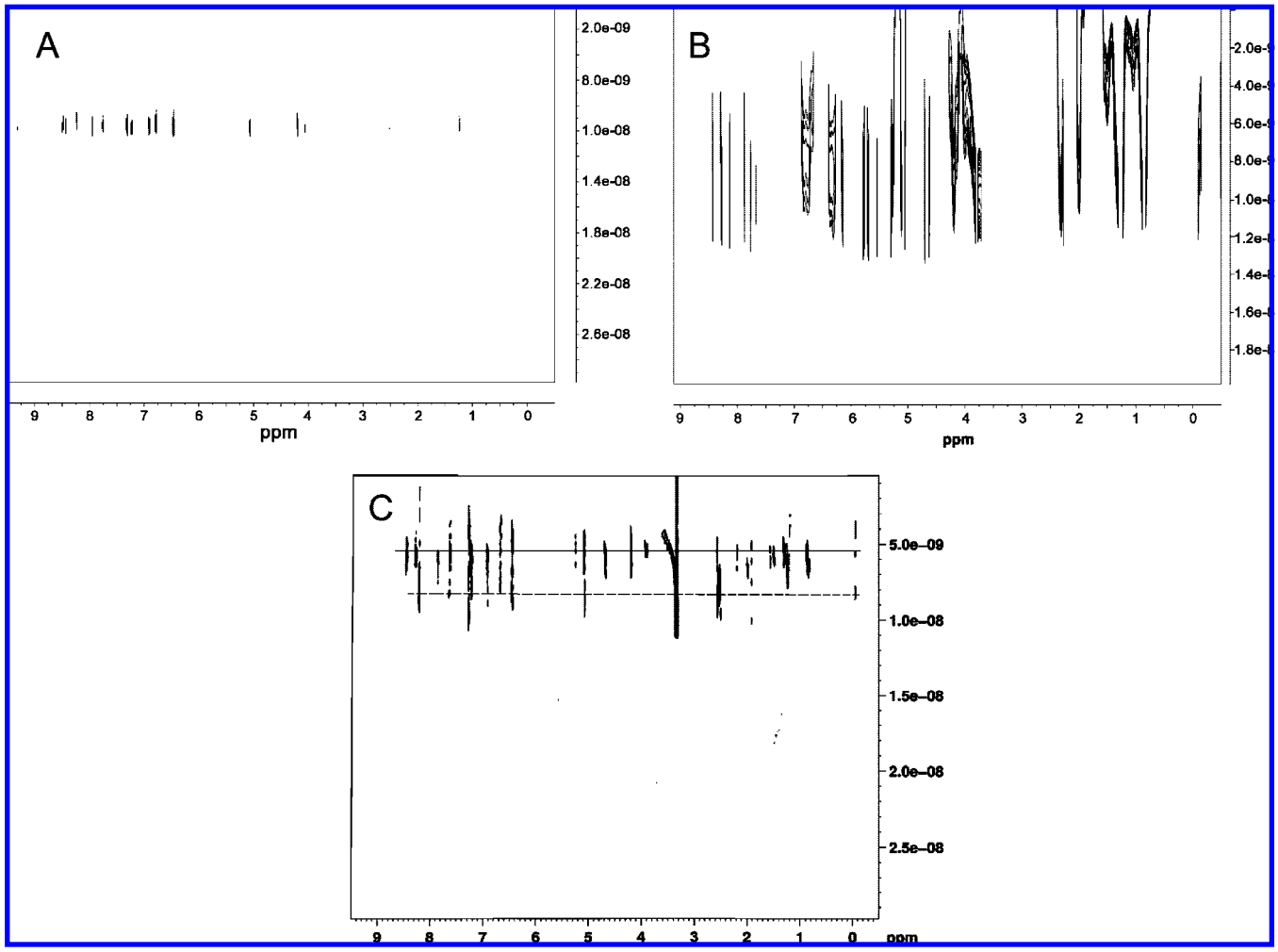


***Figure 9.*** HRMAS $^1$H DOSY 2D spectra of (A) **4**, (B) MNP4, and (C) the **4** + MNP4 mixture, acquired in DMSO at an MAS rate of 8 KHz. Continuous and dashed lines in (C) represent the mean diffusion values of the two main populations recovered in the DOSY spectrum of the mixture, which correspond to MNP4 and **4**, respectively.

of **4** and MNP4 (Figure 9). Although fine HRMAS DOSY spectra of pure MNP4 were quite difficult to obtain due to the slight inhomogeneous size dispersion of the nanoparticles, a unique band group with a substantially conserved diffusion was observed (Figure 9B), as in the case of pure ligand **4** (Figure 9A). In contrast, two partially superimposed sets of signals are evident in Figure 9C, in which the mixture of **4** and MNP4 was analyzed, one corresponding to the bound molecules and the other one referring to the free ligands.

To have further experimental evidence that no degradation occurred during ligand attachment to the particle, we checked the molecular weight by MALDI-TOF MS. The spectrum of quinoline derivative **4** showed an intense peak at 563.9 *m*/*z* with an isotopic distribution due to the presence of a chlorine atom on molecule **4**. The same intense peak at 564.0 *m*/*z* and congruent isotopic distribution were recovered within the mass spectrum of MNP4, confirming the successful attachment of the quinoline derivative to the magnetic nanoparticles (Figure S7 in the Supporting Information).

Finally, MNP3 and MNP4 were also examined by FTIR, providing further evidence of the presence of the relevant ligands in comparison with the spectra of **3** and **4**, respectively (these

results have been included in Figure S8 in the Supporting Information).

## Conclusions

The application of HRMAS to the NMR analysis of even complex organic ligands bound to paramagnetic iron oxide nanoparticles proved very successful once the experimental parameters were appropriately set up. Well-defined spectra were obtained in $^{1}$H NMR experiments, providing the first set of examples with resolved signal fine structure. 2D homonuclear $^{1}$H$-^{1}$H COSY experiments were easily performed on hybrid nanoparticles, which helped us to unambiguously attribute the peak assignments for each proton, while $^{1}$H$-^{13}$C HSQC data allowed us to extrapolate the $^{13}$C NMR chemical shifts of primary to tertiary carbons. To the best of our knowledge, this is the first example of $^{13}$C characterization of ligands bound to paramagnetic iron oxide nanoparticles. HRMAS was also successfully applied to two-dimensional DOSY, providing evidence of the ligand stability on the nanoparticle surface. Further, the comparison between $^{1}$H spectra of **4** and MNP4 prompted us to put forward a hypothesis on an unpredicted mechanism for ligand chelating to the particle surface, thus suggesting potential applications of these experiments even beyond structure elucidation. MNP3 and MNP4 were also evaluated by MALDI-TOF MS, obtaining results in good agreement with the expected molecular masses. On the whole, combining HRMAS NMR with MALDI-TOF MS provides a robust platform for the accurate, detailed, full structure characterization of organic molecules anchored onto the surface of magnetic nanocrystals. Joining the presented analytical platform with traditional FTIR analysis enabled us to handle hybrid MNP dispersions as they were a conventional organic solute, giving a conceptually innovative molecular diagnostic tool in the hands of nanochemists.

**Acknowledgment.** This paper is dedicated to Prof. Giovanni Russo on the occasion of his 70th birthday. We thank Dr. Anna Daghetti for help in the MALDI experiments and Raffaele Allevi (Sacco Hospital Facility, University of Milan) for the TEM images. The work was supported by the Regione Lombardia, an FIRB grant (CHEM-PROFARMA-NET, RBPR05NWWC), the Cariplo Foundation, the Invernizzi Foundation, and MIUR-COFIN (Grant 39903).

**Supporting Information Available:** TEM image and additional NMR, MALDI, and FTIR spectra. This material is available free of charge via the Internet at http://www.pubs.acs.org.

JA802479N